The Journal of Chemical Physics

RESEARCH ARTICLE | SEPTEMBER 28 2026

Photophysics of heteroatom-doped B,N multiple-resonance emitters: A computational investigation

Special Collection: Festschrift in honor of Yi Luo: Frontiers in Theoretical Spectroscopy, Intelligent Chemistry and Beyond

Yaxin Wang ; Wensheng Yang ; Xiaonan Ma ; Zhigang Shuai

Check for updates

J. Chem. Phys. 165, 124122 (2026)
https://doi.org/10.1063/5.0349411

View Online
Export Citation

Articles You May Be Interested In

Computational protocol for emission spectra and PLQY for thermally activated delayed fluorescence derived from sulfur/selenium-incorporated multi-resonant molecules

J. Chem. Phys. (December 2025)

Static vs Herzberg–Teller spin–orbit coupling under symmetry-reducing distortion in multi-resonance TADF emitters

J. Chem. Phys. (October 2026)

On the correlation energy features in planar heteroatomic molecular systems

J. Chem. Phys. (August 2001)

02 November 2026 09:24:40

AIP Publishing

AIP Publishing
The Journal of Chemical Physics
Special Topics Open for Submissions
Learn More

The Journal of Chemical Physics ARTICLE pubs.aip.org/aip/jcp

Photophysics of heteroatom-doped B,N multiple-resonance emitters: A computational investigation

Cite as: J. Chem. Phys. 165, 124122 (2026); doi: 10.1063/5.0349411
Submitted: 23 June 2026 • Accepted: 9 September 2026 •
Published Online: 28 September 2026

View Online Export Citation CrossMark

Yaxin Wang,[1] Wensheng Yang,[2,3] Xiaonan Ma,[2] and Zhigang Shuai[1,4,a)]

AFFILIATIONS

[1] Guangdong Basic Research Center of Excellence for Aggregate Science, School of Science and Engineering, The Chinese University of Hong Kong, Shenzhen, Guangdong 518172, People's Republic of China
[2] Institute of Molecular Plus, Tianjin University, Tianjin 300072, People's Republic of China
[3] Engineering Research Center for Nanomaterials, Henan University, Kaifeng 475004, People's Republic of China
[4] MOE Key Laboratory of Organic OptoElectronics and Molecular Engineering, Department of Chemistry, Tsinghua University, 100084 Beijing, People's Republic of China

Note: This paper is part of the Festschrift in Honor of Yi Luo: Frontiers in Theoretical Spectroscopy, Intelligent Chemistry and Beyond.

[a)] **Author to whom correspondence should be addressed:** shuaizhigang@cuhk.edu.cn

ABSTRACT

Boron/nitrogen multiple-resonance thermally activated delayed fluorescence (B/N MR-TADF) emitters offer high color purity, but accelerating reverse intersystem crossing (RISC) without sacrificing narrowband emission remains challenging. Here, 16 C-, O-, S-, and Se-containing B/N MR-TADF emitters with varied framework symmetries are investigated using density functional theory (DFT), time-dependent density functional theory (TD-DFT), and the thermal vibration correlation function (TVCF) formalism. We find that the conventional $T_1 \rightarrow S_1$ pathway cannot explain the accelerated RISC because the S_1–T_1 gap remains thermally unfavorable. Instead, a near-resonant high-lying T_2 state provides an intrinsically fast spin-conversion pathway, although its productive contribution is governed by the competition between $T_2 \rightarrow S_1$ RISC and $T_2 \rightarrow T_1$ internal conversion. Chalcogen embedding and framework symmetry breaking cooperatively tune the T_2 orbital character, enhance S_1–T_2 spin–orbit coupling (SOC), and yield direct $T_2 \rightarrow S_1$ RISC rate constants from 8.65×10^7 to 8.77×10^9 s^{-1} for S- and Se-containing emitters with numerically stable T_2-state vibronic parameters. Spectral simulations further show that the same heavy-atom perturbation can increase S_1/S_0 relaxation, reorganization energy, and vibronic coupling, thereby broadening emission. The emission bandwidth correlates more closely with $S_1 \rightarrow S_0$ reorganization energy than with global structural displacement, identifying vibronic reorganization as the key color-purity descriptor. Thus, S_1–T_2 energy alignment and SOC govern the intrinsic spin-conversion capability, whereas framework rigidity, symmetry, and reorganization energy determine narrowband emission. Symmetric double locking with localized S or Se embedding, therefore, provides a practical strategy for balancing intrinsic spin-conversion capability and color purity.

Published under an exclusive license by AIP Publishing. https://doi.org/10.1063/5.0349411

I. INTRODUCTION

Organic light-emitting diodes (OLEDs) for high-resolution and ultrahigh-definition displays require emitters that simultaneously deliver efficient exciton utilization and high color purity.[1–5] Thermally activated delayed fluorescence (TADF) enables metal-free triplet exciton harvesting through reverse intersystem crossing (RISC), but conventional donor–acceptor TADF emitters usually reduce the singlet–triplet energy gap by spatially separating frontier molecular orbitals over flexible donor and acceptor fragments.[6–10] Although this strategy improves exciton utilization, it often enhances excited-state structural relaxation and electron–vibration coupling, producing broad emission profiles that compromise display color purity and may require optical filtering

02 November 2026 09:24:40

Published under an exclusive license by AIP Publishing

or microcavity engineering.[5,10–17] Therefore, the central molecular-design challenge is to boost intrinsic delayed fluorescence without sacrificing the narrow emission bandwidth.

Boron/nitrogen multiple-resonance (B/N MR)-TADF emitters address the color-purity aspect of this challenge by combining short-range charge-transfer (SRCT) excited-state character with a rigid polycyclic framework.[18–21] The archetypal MR-TADF emitter, 5,9-diphenyl-5,9-diaza-13b-boranaphtho[3,2,1-de]anthracene (DABNA-1), was first reported by Hatakeyama *et al.* in 2016.[18] In DABNA-type frameworks, the antiphase resonance effects of electron-deficient boron and electron-rich nitrogen atoms enable atomic-scale separation of the highest occupied molecular orbital (HOMO) and lowest unoccupied molecular orbital (LUMO) without introducing a strongly twisted donor–acceptor geometry.[18,19] This unique electronic configuration suppresses bonding and antibonding structural relaxation and high-frequency vibronic coupling, giving narrowband emission with small Stokes shifts.[14,15,20,22–27] However, the same localized MR electronic structure generally gives weak spin–orbit coupling (SOC) and unfavorable excited-state energy-level alignment, so many B/N MR-TADF emitters still show modest intrinsic RISC rate constants, typically on the order of 10^3–10^4 s^{-1}.[15,27–29] Slow triplet-to-singlet upconversion lengthens triplet lifetimes and promotes triplet–triplet and triplet–polaron annihilation under practical current densities, leading to severe efficiency roll-off.[10,13] Thus, B/N MR-TADF emitters exhibit an intrinsic mechanistic tension between the rigid, symmetry-regulated framework required for color purity and the spin-mixing interactions required for efficient triplet harvesting.

Heavy-atom embedding and framework locking provide two structural handles for tuning this tension, but their photophysical roles are configuration-dependent rather than independent. Introducing nonmetallic heavy atoms, especially group-16 atoms, such as sulfur and selenium, can enhance SOC through an internal heavy-atom effect and has led to experimentally observed delayed-fluorescence acceleration and reduced efficiency roll-off in several MR-TADF emitters.[30–38] At the same time, peripheral locking, framework extension, and asymmetric protection can modulate frontier-orbital distributions, molecular rigidity, and excited-state structural relaxation.[39–50] Recent sulfur- and selenium-containing MR-TADF emitters demonstrate that fast delayed fluorescence and relatively narrow emission can coexist, yet other heavy-atom or asymmetric modifications broaden emission by enhancing S_1/S_0 relaxation and vibronic shoulder features.[27,28,31–35] These observations indicate that atomic number alone is not a sufficient design descriptor; the global symmetry and rigidity of the B/N framework determine whether a local heavy-atom perturbation improves efficiency, degrades color purity, or balances both.

The microscopic origin of this balance remains unresolved because RISC in MR-TADF emitters is often interpreted using an oversimplified lowest-triplet $T_1 \rightarrow S_1$ picture. According to Fermi's golden rule, RISC depends on both singlet–triplet energy separation and SOC.[6,12,29,51] For MR frameworks, however, the S_1–T_1 gap is often difficult to reduce without perturbing the emissive framework, and heavy-atom-enhanced S_1–T_1 SOC alone may not overcome this energetic penalty. Several low-lying triplet states can lie close to S_1, so a high-lying triplet state may provide a more efficient spin-conversion channel when its energy, orbital character, and SOC are simultaneously favorable.[26,27,29,37,51–55] It is, therefore, necessary to determine which triplet state controls the operative RISC channel, how heavy atoms and framework symmetry reshape the relevant orbital characters, and which structural descriptors govern the accompanying loss of color purity. A unified analysis of excited-state ordering, SOC, RISC kinetics, S_1/S_0 structural relaxation, reorganization energy, and mode-resolved vibronic coupling is required to convert these qualitative design concepts into experimentally useful guidelines.[17,56]

In this work, we systematically investigate 16 DABNA-derived B/N MR-TADF emitters designed to decouple embedded-atom identity from framework locking configuration. By combining density functional theory (DFT), time-dependent (TD)-DFT, SOC calculations, natural transition orbital (NTO) analysis, and thermal vibration correlation function (TVCF) simulations, we identify how heavy-atom effects and molecular symmetry jointly regulate the efficiency–color-purity trade-off. The results demonstrate that a high-lying T_2 channel can provide a fast intrinsic spin-conversion pathway beyond the conventional T_1 channel, but its productive contribution is limited by the competing $T_2 \rightarrow T_1$ internal-conversion pathway. Heavy-atom embedding and symmetry breaking strengthen S_1–T_2 SOC and generate large $T_2 \rightarrow S_1$ RISC rate constants, whereas excessive asymmetry and large chalcogen atoms increase S_1/S_0 reorganization energy and broaden emission. The symmetric doubly locked S- and Se-containing frameworks, therefore, emerge as balanced candidates because they retain a strong intrinsic high-lying-triplet spin-conversion capability while suppressing the structural relaxation responsible for color-purity loss. These findings establish molecular descriptors for experimental design: S_1–T_2 energy-level alignment and SOC determine the intrinsic triplet spin-conversion capability, whereas the rates governing T_2 population and depletion, together with framework rigidity, symmetry, and $S_1 \rightarrow S_0$ reorganization energy, determine whether narrowband MR emission is retained.

II. METHODOLOGY

Photophysical properties were evaluated by combining electronic-structure calculations with the TVCF formalism. The spectra and radiative rate constants were calculated at the zeroth-order Franck–Condon level, for which the electronic transition dipole moment is assumed to be independent of the nuclear coordinates. Herzberg–Teller corrections arising from nuclear-coordinate derivatives of the transition dipole moment were, therefore, not included. This approximation is appropriate because the S_1–S_0 transitions considered here are electric-dipole allowed and because the analysis focuses on relative spectral trends and structure–property relationships across the molecular series. The detailed derivations and solutions of the governing equations are available in previous studies.[57–63]

A. Optical spectra

Within Fermi's golden rule and the Franck–Condon (FC) approximation, the vibrationally resolved absorption cross section from electronic state i to f can be written as

$$\sigma_{ab}(\omega, T) = \frac{4\pi^2\omega}{3\hbar c}\left|\boldsymbol{\mu}_{fi}\right|^2 \sum_{u,v} P_{iv}\left|\langle\Theta_{fu}|\Theta_{iv}\rangle\right|^2 \delta(\omega - \omega_{fu,iv}), \quad (1)$$

02 November 2026 09:24:40

Published under an exclusive license by AIP Publishing

$$\sigma_{\mathrm{em}}(\omega,T)=\frac{4\omega^3}{3\hbar c^3}\left|\boldsymbol{\mu}_{\mathrm{fi}}\right|^2\sum_{u,v}P_{iv}\left|\langle\Theta_{fu}|\Theta_{iv}\rangle\right|^2\delta(\omega_{iv,fu}-\omega). \tag{2}$$

Here, $\hbar$ is the reduced Planck constant, c is the speed of light, ω is the photon angular frequency, P_{iv} is the Boltzmann population of the initial-state vibronic level, $Z_{\mathrm{i}}=\mathrm{Tr}[\mathrm{e}^{-\beta\hat{H}_{\mathrm{i}}}]$ is the corresponding vibrational partition function, and $\beta=(k_{\mathrm{B}}T)^{-1}$. Θ_{iv} and Θ_{fu} are the vibrational wave functions of the initial and final electronic states. The transition dipole moment $\boldsymbol{\mu}_{\mathrm{fi}}=\langle\Phi_{\mathrm{f}}|\hat{\boldsymbol{\mu}}|\Phi_{\mathrm{i}}\rangle$ is treated as independent of the nuclear coordinates under the FC approximation.

By applying the time-dependent TVCF formalism, Eqs. (1) and (2) can be recast as

$$\sigma_{\mathrm{ab}}^{\mathrm{FC}}(\omega,T)=\frac{2\pi\omega}{3\hbar c}\left|\boldsymbol{\mu}_{\mathrm{fi}}\right|^2\int_{-\infty}^{\infty}\mathrm{e}^{\mathrm{i}(\omega-\omega_{\mathrm{fi}})t}\rho_{\mathrm{ab},0}^{\mathrm{FC}}(t,T)\,\mathrm{d}t, \tag{3}$$

$$\sigma_{\mathrm{em}}^{\mathrm{FC}}(\omega,T)=\frac{2\omega^3}{3\pi\hbar c^3}\left|\boldsymbol{\mu}_{\mathrm{fi}}\right|^2\int_{-\infty}^{\infty}\mathrm{e}^{-\mathrm{i}(\omega-\omega_{\mathrm{if}})t}\rho_{\mathrm{em},0}^{\mathrm{FC}}(t,T)\,\mathrm{d}t. \tag{4}$$

The absorption and emission TVCFs have the same form

$$\rho_{\alpha,0}^{\mathrm{FC}}(t,T)=Z_{\mathrm{i}}^{-1}\mathrm{Tr}\left[\mathrm{e}^{-\mathrm{i}\tau_{\mathrm{f}}\hat{H}_{\mathrm{f}}}\mathrm{e}^{-\mathrm{i}\tau_{\mathrm{i}}\hat{H}_{\mathrm{i}}}\right], \tag{5}$$

where α = ab or em and $\hat{H}_{\mathrm{i}}$ and $\hat{H}_{\mathrm{f}}$ are the vibrational Hamiltonians of the initial and final electronic states, respectively. The complex time variables in Eq. (5) are defined as $\tau_{\mathrm{f}}=t/\hbar$ and $\tau_{\mathrm{i}}=-\mathrm{i}\beta-\tau_{\mathrm{f}}$. In addition, the initial- and final-state normal coordinates are related by the Duschinsky transformation,

$$Q_{ik}=\sum_{l=1}^{N}S_{\mathrm{i}\leftarrow\mathrm{f},kl}Q_{fl}+\underline{D}_{\mathrm{i}\leftarrow\mathrm{f},k}, \tag{6}$$

where Q_{ik} and Q_{fl} are the kth and lth components of the initial- and final-state normal coordinates, respectively. The Duschinsky rotation matrix and displacement vector are then defined as $\boldsymbol{S}_{\mathrm{i}\leftarrow\mathrm{f}}=\boldsymbol{L}_{\mathrm{i}}^{\mathrm{T}}\boldsymbol{L}_{\mathrm{f}}$ and $\underline{D}_{\mathrm{i}\leftarrow\mathrm{f}}=\boldsymbol{L}_{\mathrm{i}}^{\mathrm{T}}\left(\boldsymbol{q}_{\mathrm{f}}^{0}-\boldsymbol{q}_{\mathrm{i}}^{0}\right)$, respectively. In addition, bold variables represent square matrices and underlined variables represent column matrices. Within the harmonic oscillator model, distortion of the final-state potential-energy surface corresponds to the changes of the normal-mode frequencies relative to those of the initial electronic state.

B. Radiative and nonradiative decay rate constants

Under the FC approximation, the radiative decay rate constant in our work is given by

$$k_{\mathrm{r}}(T)=\int_{0}^{\infty}\sigma_{\mathrm{em}}^{\mathrm{FC}}(\omega,T)\,\mathrm{d}\omega. \tag{7}$$

Accordingly, the total internal conversion (IC) rate between two electronic states with the same spin multiplicity can be expressed as

$$k_{\mathrm{IC}}(T)=\frac{1}{\hbar^2}\sum_{k,l}R_{kl}\int_{-\infty}^{\infty}\mathrm{d}t\;\mathrm{e}^{\mathrm{i}\omega_{\mathrm{if}}t}Z_{\mathrm{i}}^{-1}\rho_{\mathrm{IC},kl}(t,T), \tag{8}$$

where $R_{kl}=\left\langle\Phi_{\mathrm{f}}|\hat{P}_{fk}|\Phi_{\mathrm{i}}\right\rangle\left\langle\Phi_{\mathrm{i}}|\hat{P}_{fl}|\Phi_{\mathrm{f}}\right\rangle$ is the product of the nonadiabatic electronic coupling matrix elements associated with final-state normal modes k and l. Here, $\hat{P}_{fk}$ denotes the nuclear momentum operator associated with final-state mode k, and Z_{i} is the vibrational partition function of the initial electronic state defined above. The corresponding IC time-correlation function is $\rho_{\mathrm{IC},kl}(t,T)=\mathrm{Tr}\left[\hat{P}_{fk}\mathrm{e}^{-\mathrm{i}\tau_{\mathrm{f}}\hat{H}_{\mathrm{f}}}\hat{P}_{fl}\mathrm{e}^{-\mathrm{i}\tau_{\mathrm{i}}\hat{H}_{\mathrm{i}}}\right]$.

For spin-forbidden transitions, the intersystem crossing (ISC) and RISC rate constants were calculated by replacing the nonadiabatic coupling term with the SOC matrix element,

$$k_{\mathrm{ISC}}(T)=\frac{\left|\left\langle\Phi_{\mathrm{f}}|\hat{H}_{\mathrm{SO}}|\Phi_{\mathrm{i}}\right\rangle\right|^2}{\hbar^2}\int_{-\infty}^{\infty}\mathrm{e}^{\mathrm{i}\omega_{\mathrm{if}}t}Z_{\mathrm{i}}^{-1}\rho_{\mathrm{ISC}}(t,T)\,\mathrm{d}t, \tag{9}$$

where $\rho_{\mathrm{ISC}}(t,T)=\mathrm{Tr}\left[\mathrm{e}^{-\mathrm{i}\tau_{\mathrm{f}}\hat{H}_{\mathrm{f}}}\mathrm{e}^{-\mathrm{i}\tau_{\mathrm{i}}\hat{H}_{\mathrm{i}}}\right]$ is the corresponding ISC time-correlation function. The same correlation-function formalism was used for both ISC and RISC by interchanging the initial and final electronic states. However, the ISC and RISC rates differ in the statistical treatment of the three spin sublevels associated with each triplet state. For $S_1\rightarrow T_n$ ISC, the reported rate is obtained by summing the three sublevel-specific rates because the sublevels constitute distinct final-state channels. For $T_n\rightarrow S_1$ RISC, assuming equal populations of the three triplet spin sublevels, the reported rate is obtained by averaging the corresponding sublevel-specific rates.

For clarity, the relaxation rates used below are defined on a state-to-state basis. For the S_1 manifold, $k_{\mathrm{r}}\equiv k_{\mathrm{r}}(S_1\rightarrow S_0)$ denotes fluorescence, whereas $k_{\mathrm{nr}}\equiv k_{\mathrm{IC}}(S_1\rightarrow S_0)$ denotes same-spin IC. The $S_1\rightarrow T_1$ and $S_1\rightarrow T_2$ ISC rates are treated separately and are not included in k_{nr}. For the triplet manifold, $k_{\mathrm{rt}}\equiv k_{\mathrm{r}}(T_1\rightarrow S_0)$ denotes phosphorescence, whereas $k_{\mathrm{nrt}}\equiv k_{\mathrm{ISC}}(T_1\rightarrow S_0)$ denotes nonradiative spin-forbidden $T_1\rightarrow S_0$ decay evaluated using the SOC-based TVCF formalism. The $T_1\rightarrow S_1$ and $T_2\rightarrow S_1$ RISC channels and the $T_2\leftrightarrow T_1$ IC processes are treated explicitly as separate state-to-state transitions and are not included in k_{nrt}.

The $T_n\rightarrow S_1$ RISC rate constants introduced above describe state-specific spin-conversion channels. Given the multiple RISC pathways available in the investigated emitters, we employ a Boltzmann-weighted effective RISC rate as a comparative descriptor under the T_1/T_2 thermal-equilibrium approximation. The resulting effective RISC rate constant was defined as

$$k_{\mathrm{RISC}}^{\mathrm{eff}}=\frac{k_{\mathrm{RISC}}^{\mathrm{T_1}\rightarrow\mathrm{S_1}}+k_{\mathrm{RISC}}^{\mathrm{T_2}\rightarrow\mathrm{S_1}}\mathrm{e}^{-\frac{E_{\mathrm{T_2}}-E_{\mathrm{T_1}}}{k_{\mathrm{B}}T}}}{1+\mathrm{e}^{-\frac{E_{\mathrm{T_2}}-E_{\mathrm{T_1}}}{k_{\mathrm{B}}T}}}. \tag{10}$$

This expression assumes thermal equilibration between T_1 and T_2 before upconversion and represents a normalized Boltzmann-population-weighted average of the state-specific $T_1\rightarrow S_1$ and $T_2\rightarrow S_1$ RISC rates. Because T_1 and T_2 have the same threefold spin degeneracy, the common degeneracy factor cancels upon normalization.

C. Computational details

The ground-state (S_0) geometry was optimized using DFT, whereas the S_1, T_1, and T_2 excited-state geometries were independently optimized using TD-DFT, as implemented in Gaussian 16.[64] All geometry optimizations were performed at the B3LYP/6-311G** level with the polarizable continuum model (PCM) for toluene. Harmonic-frequency calculations were performed at the

02 November 2026 09:24:40

Published under an exclusive license by AIP Publishing

corresponding optimized geometries to verify the stationary points as local minima. The electronic characters of the optimized S_1, T_1, and T_2 states were further examined by TD-DFT and NTO analysis to ensure consistent state assignment. Before the production calculations, a functional benchmark was performed for representative experimentally reported O-, S-, and Se-containing B/N MR-TADF emitters related to the present molecular frameworks.[15,25,26,32–34] Twelve commonly used functionals, namely PBE0, B3LYP, TPSSh, BMK, BHandHLYP, M06HF, M06-2X, CAM-B3LYP, LC-BLYP, LC-ωPBE, ωB97X, and ωB97XD, were examined with the same 6-311G** basis set and PCM with toluene as the solvent. The calculated emission energies were compared with the corresponding experimental solution photoluminescence maxima. As summarized in Table S1 in the supplementary material, B3LYP gives the smallest overall deviation from experiment, with a mean absolute error of 0.046 eV for the tested emitters. PBE0 provides the next-best agreement with a larger mean absolute error of 0.073 eV, whereas the long-range-corrected functionals systematically overestimate the emission energies. Therefore, the B3LYP functional with the 6-311G** basis set was employed for geometry optimizations and excited-state calculations. Because the calculated quantities are vertical emission energies whereas the experimental data correspond to solution photoluminescence maxima, this comparison is used as an empirical benchmark of the overall emission-energy scale rather than as a one-to-one validation of vibronically resolved peak positions. This computational level was chosen to provide an internally consistent comparison across the C, O, S, and Se series.

Adiabatic excited-state energies were obtained from the individually optimized S_1, T_1, and T_2 geometries at the TD-DFT/B3LYP/6-311G**/PCM (toluene) level. The electronic character of each optimized excited state was verified by NTO/state-character analysis. Accordingly, all S_1–T_1 and S_1–T_2 gaps discussed in the main text were evaluated from the corresponding relaxed-state energies and represent adiabatic energy differences. These adiabatic gaps were used as the energetic inputs and operational descriptors for the corresponding TVCF rate calculations. For MR-TADF emitters, differential treatment of electron correlation in the singlet and triplet states can make the calculated energy gaps method-dependent, as discussed by Hall *et al.*[65] The present TD-DFT protocol is used to identify systematic relative trends rather than to provide spectroscopic-accuracy predictions of absolute energy gaps and state orderings or quantitatively validated absolute RISC rates. Higher-level wavefunction methods, such as spin-component-scaled second-order approximate coupled-cluster singles-and-doubles (SCS-CC2) or spin-component-scaled second-order algebraic-diagrammatic construction [SCS-ADC(2)], and suitable double-hybrid approaches could provide more quantitative predictions of individual gaps and state orderings. Cases with $|\Delta E_{S_1-T_2}| \lesssim 0.10$ eV are treated as near-resonant rather than as definitive state-order predictions; this threshold is pragmatic within the employed protocol and is not an estimate of the TD-DFT error. Accordingly, the mechanistic assignment below is based on the combined behavior of energy gaps, NTO characters, SOC matrix elements, and competing rate constants, rather than on a single calculated excitation energy.

SOC matrix elements between relevant singlet and triplet states were calculated using the PySOC program.[66] The S_1–T_n SOC matrix elements for ISC were evaluated at the optimized S_1 geometry, whereas the T_n–S_1 SOC matrix elements for RISC were evaluated at the corresponding independently optimized T_n geometry ($n = 1, 2$). For S- and Se-containing molecules, the SOC values are interpreted as comparative nonmetallic heavy-atom descriptors within the same electronic-structure protocol. Although this perturbative treatment captures the expected increase in SOC from O to S to Se, quantitative SOC values for Se may be affected by scalar-relativistic, SOC, and basis-set effects that are not exhaustively benchmarked here. The mechanistic conclusions below, therefore, rely on internally consistent trends that combine the energy gap, state character, and rate competition rather than on a single absolute SOC number. NTO analysis was used to characterize the electronic nature of the low-lying excited states, and hole–electron analysis was performed using Multiwfn.[67]

Radiative decay, internal conversion, ISC, RISC, and vibrationally resolved absorption and emission spectra were simulated at 300 K using the Molecular Materials Property Prediction Package (MOMAP),[57–60,62,63] without additional phenomenological broadening. Normal-mode displacement, frequency distortion, and Duschinsky rotation effects were included. The $S_1 \rightarrow S_0$ reorganization energy, denoted by Γ, was decomposed into normal-mode contributions, and Huang–Rhys factors were used to quantify mode-resolved vibronic coupling. Root-mean-square displacement (RMSD) values between the optimized S_0 and S_1 geometries were calculated after structural alignment to evaluate the overall excited-state structural relaxation. The calculated spectra correspond to isolated molecules in a continuum toluene environment. Thus, the emission maxima and full width at half maximum (FWHM) values are used to compare intrinsic molecular broadening trends. Explicit host packing, aggregation, exciton–phonon coupling in the solid state, and optical microcavity effects are not included; comparison with available experiments is, therefore, restricted to qualitative trends in emission shift and bandwidth rather than to one-to-one prediction of film FWHM values. For the T_2 states of S-3 and Se-3, although the optimized geometries were confirmed to be local minima by harmonic frequency analysis, the subsequent electron–vibration coupling (EVC) and TVCF calculations yielded $T_2 \rightarrow S_1$ reorganization energies that were substantially larger than those of the other compounds in the series, with the anomalous contribution mainly concentrated in a single high-frequency mode. Despite repeated attempts using different initial guess structures and tighter convergence criteria, this numerical issue persisted. Therefore, although these optimized T_2 structures formally satisfy the conventional local-minimum criterion, we consider the subsequent T_2-dependent quantitative treatment insufficiently robust for reliable kinetic analysis under the present protocol. Accordingly, the quantitative data that depend on these optimized T_2 structures are excluded from the present quantitative analysis. Quantities evaluated independently of the problematic T_2-state treatment are retained where available.

III. RESULTS AND DISCUSSION

Experimentally, several molecular-engineering strategies have been developed to regulate the photophysical behavior of B/N MR-TADF emitters. As summarized in Fig. 1(a), BCz-BN-type framework extension has been used to tune excited-state energy-level alignment, 2PTZ-BN-type chalcogen embedding has been

02 November 2026 09:24:40

Published under an exclusive license by AIP Publishing

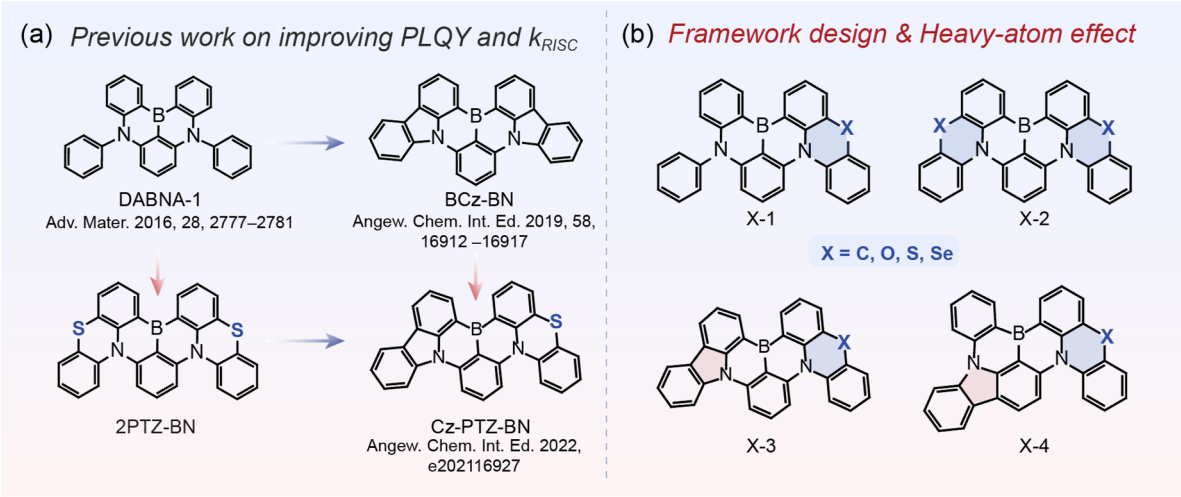


FIG. 1. Molecular structures and naming scheme of the investigated B/N MR-TADF emitters. Here, X denotes C, O, S, or Se; X-1 is an asymmetric singly locked structure; X-2 is a symmetric doubly locked structure; and X-3 and X-4 are asymmetric doubly locked structures.

introduced to strengthen SOC, and the asymmetric Cz-PTZ-BN framework has been proposed to examine whether these two effects can be coupled within one MR scaffold. Inspired by these experimentally accessible motifs, we constructed the molecular set shown in Fig. 1(b) to disentangle the configuration-dependent roles of heavy-atom embedding, framework symmetry, and structural rigidity in determining color purity and RISC kinetics. The molecules are labeled X–Y, where X represents C, O, S, or Se and Y specifies the locking configuration. In particular, X–1 denotes an asymmetric singly locked framework, whereas X–2 denotes a symmetric doubly locked framework. X–3 and X–4 represent two distinct asymmetric doubly locked frameworks. Within each locking configuration, the C–Y series serves as the non-heavy-atom reference. The corresponding O–Y, S–Y, and Se–Y series incorporate group-16 atoms with increasing nuclear charge and progressively stronger nonmetallic heavy-atom effects. This matrix-like molecular design enables direct structure–property comparison of energy-level alignment, SOC, framework symmetry, and excited-state relaxation within the same B/N MR platform.

A. Relaxation channels

In conventional TADF analysis, RISC is usually discussed through the lowest triplet channel, $T_1 \rightarrow S_1$. According to Fermi's golden rule, the RISC rate depends not only on the energy gap but also on the strength of the SOC matrix element.[6,12,29,51] Therefore, we first evaluated the adiabatic S_1–T_1 gaps, S_1–T_1 SOC matrix elements, and the corresponding RISC rate constants. As summarized in Table S2(a) in the supplementary material, replacing the carbon bridge with embedded chalcogen atoms modulates the S_1–T_1 SOC, with the magnitude of the change depending on the locking configuration. For a given locking configuration, the SOC generally increases toward the heavier Se analog, although configuration-dependent deviations are present. This enhancement is particularly evident in the asymmetric frameworks: Se-4 gives an S_1–T_1 SOC of 1.37 cm^{-1}, much larger than that of C-4 (0.24 cm^{-1}), whereas the symmetric Se-2 analog gives a smaller value of 0.11 cm^{-1}. Thus, the heavy-atom effect is not an atom-only descriptor; it is strongly modulated by the molecular framework because symmetry breaking reshapes the electronic wave functions involved in spin conversion.

The S_1–T_1 channel alone, however, cannot account for the calculated RISC behavior. Although the S_1–T_1 SOC is enhanced by heavy-atom embedding, the adiabatic S_1–T_1 gaps remain relatively large. Even for the X-3 series, which has the smallest S_1–T_1 gaps, $\Delta E_{S_1-T_1}$ ranges from 0.30 to 0.40 eV, whereas the X-4 series gives values of ~0.39–0.47 eV. As a result, the calculated $T_1 \rightarrow S_1$ RISC rate constants range from 10^0 to 10^3 s^{-1}. Moreover, the largest $T_1 \rightarrow S_1$ rate appears for the carbon reference C-3 (1.97×10^3 s^{-1}), rather than for the Se-containing molecules. This non-monotonic behavior reflects the fact that the RISC rate is governed not only by the energy gap and SOC but also by the state-specific vibronic contribution contained in the TVCF correlation function; therefore, the comparatively high $T_1 \rightarrow S_1$ RISC rate of C-3 cannot be inferred from $\Delta E_{S_1-T_1}$ and SOC alone. This result indicates that experimentally relevant heavy-atom-promoted RISC cannot be rationalized by a simple two-state S_1/T_1 model.

We then examined the higher triplet manifold to identify its contribution to the operative multistate spin-conversion network. As shown in Fig. 2(a), the available S_1–T_2 gaps are much smaller than the S_1–T_1 gaps and range from −0.17 to 0.09 eV, indicating that T_2 is nearly resonant with S_1 in most molecular scaffolds. The complete S_0, S_1, T_1, and T_2 energy-level distributions are provided in Fig. S1 in the supplementary material. Because these separations are small on the scale of the uncertainty associated with TD-DFT, the mechanistic assignment is not based on the exact sign of an individual S_1–T_2 gap. Although the T_2 geometries were independently optimized and their electronic characters were verified by NTO analysis, the absolute S_1–T_2 energy differences and detailed state ordering remain method-dependent. Therefore, we regard T_2

02 November 2026 09:24:40

Published under an exclusive license by AIP Publishing

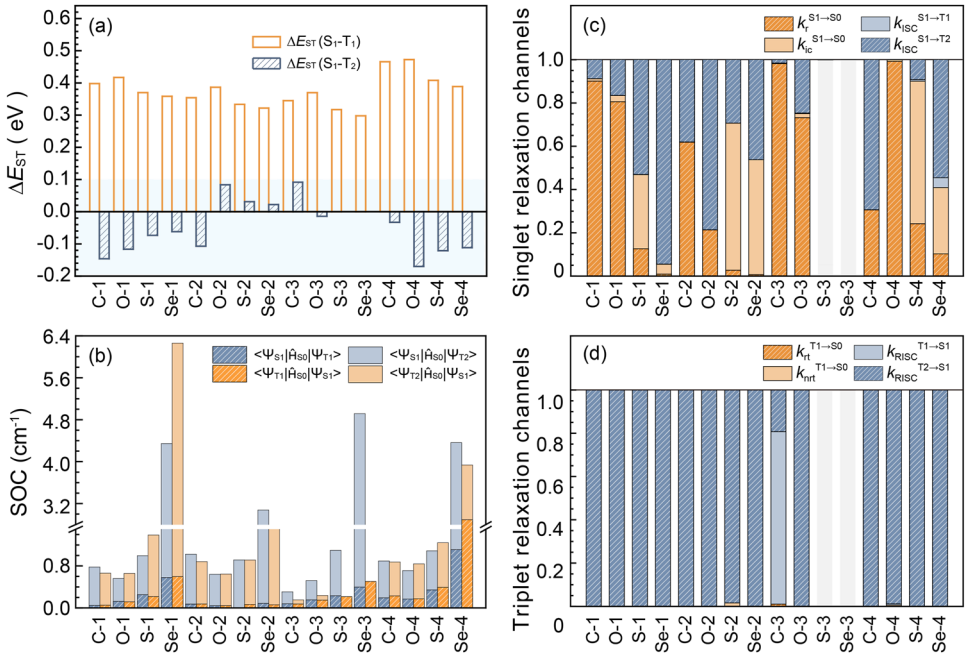


FIG. 2. Calculated excited-state energy gaps, SOC matrix elements, and relaxation channels of the investigated B/N MR-TADF emitters. (a) Adiabatic S_1–T_1 and S_1–T_2 energy gaps; (b) SOC matrix elements associated with S_1–T_1 and S_1–T_2 spin conversion; (c) relative contributions of radiative decay, internal conversion, $S_1 \rightarrow T_1$ ISC, and $S_1 \rightarrow T_2$ ISC to the total S_1 relaxation rate at 300 K; and (d) comparison of selected state-specific triplet decay and RISC rate constants at 300 K. The $T_2 \leftrightarrow T_1$ IC rates are not included in panel (d) and are reported separately in Table S2(c). The unavailable T_2-related data for S-3 and Se-3 are omitted from the corresponding panels; the available $S_1 \rightarrow T_2$ SOC values are retained in panel (b) (see Sec. II C and Table S2).

as a near-resonant and potentially accessible member of the low-lying triplet manifold when $|\Delta E_{S_1-T_2}| \lesssim 0.1$ eV and assess its kinetic relevance using the combined energy-gap, state-character, SOC, and rate-constant criteria. The location of T_2 is sensitive to both the embedded atom and the locking configuration. In the symmetric X-2 framework, T_2 remains close in energy to S_1, whereas T_1 lies substantially lower. In the asymmetric X-1, X-3, and X-4 frameworks, T_2 is also close to S_1 and can even become slightly higher than S_1, whereas T_1 remains clearly lower in energy. The S- and Se-containing members generally have smaller S_1–T_1 gaps than the C and O analogues, whereas the T_2 response depends more strongly on molecular symmetry. This state ordering suggests that the high-lying triplet manifold should not be treated as a passive spectator when evaluating multistate spin-conversion dynamics.

Electronic-structure analysis further clarifies the orbital origin of the enhanced SOC. The NTO hole–electron distributions and corresponding dominant transition characters for all investigated emitters are provided in Figs. S2 and S3 in the supplementary material. The percentages shown in these figures denote the weights of the dominant NTO hole–electron pairs. Compared with S_1, the T_2 state exhibits substantially different hole distributions, particularly around the heteroatom-containing and peripheral locking units. This distinct electronic character induces a larger change in orbital angular momentum, consistent with an El-Sayed-type spin-conversion pathway, and therefore gives rise to stronger S_1–T_2 SOC [Fig. 2(b)]. The corresponding SOC matrix elements are summarized in Table S2(b). For S-containing structures, the S_1–T_2 SOC values range from 0.92 to 1.10 cm^{-1}, whereas Se-containing structures exhibit larger values of 3.07–4.92 cm^{-1}. The reverse T_2–S_1 SOC matrix elements show the same enhancement, reaching 0.91–1.40 cm^{-1} for S-1, S-2, and S-4 and 2.72–6.26 cm^{-1} for Se-1, Se-2, and Se-4. For S-3 and Se-3, only the S_1–T_2 SOC matrix elements are retained because the reverse quantities depend on the optimized T_2 structures, whose subsequent quantitative treatment is not sufficiently robust under the present computational protocol. These values indicate that chalcogen identity strongly modulates the S_1/T_2 SOC, while the variations within each series reflect the influence of the molecular framework. When combined with the near-resonant S_1/T_2 energy alignment, these SOC trends support the involvement of the higher triplet manifold in spin conversion and, therefore, favor a multistate description involving both T_1 and T_2, rather than a conventional lowest-triplet-only picture.

For clarity, Fig. 2(c) shows the relative contributions of the four S_1-originating relaxation channels, whereas Fig. 2(d) compares the magnitudes of selected state-specific triplet decay and RISC rates. The asymmetric C-1, O-1, C-3, O-3, and O-4 emitters exhibit particularly high $S_1 \rightarrow S_0$ radiative decay rates, indicating a substantial radiative contribution to their S_1 relaxation and supporting favorable photoluminescence quantum yields. Within the triplet-state manifold, the $T_2 \rightarrow S_1$ RISC rate exceeds both $k_{rt}^{T_1 \rightarrow S_0}$ and $k_{nrt}^{T_1 \rightarrow S_0}$ for all molecules with reliable T_2-state vibronic parameters. We then quantified the competition among the individual excited-state pathways. As shown in Fig. 3(a), the calculated $S_1 \rightarrow T_2$ ISC rate is larger than the corresponding $S_1 \rightarrow T_1$ ISC rate for all 14 molecules included in the quantitative T_2 analysis, indicating that direct population transfer into T_2 is kinetically accessible. However, once T_2 is populated, $k_{IC}^{T_2 \rightarrow T_1}$ ranges from 7.01×10^{11} to 2.48×10^{12} s^{-1}, whereas $k_{RISC}^{T_2 \rightarrow S_1}$ ranges from 4.78×10^{2} to 8.77×10^{9} s^{-1}. The largest rate ratio, $k_{RISC}^{T_2 \rightarrow S_1}/k_{IC}^{T_2 \rightarrow T_1}$, is 3.95×10^{-3} for Se-1; therefore, direct $T_2 \rightarrow S_1$ RISC does not compete with $T_2 \rightarrow T_1$ IC for any of these molecules [Table S2(c)]. Furthermore, the reverse $T_1 \rightarrow T_2$ IC rates, obtained from detailed balance at 300 K, range from 1.38×10^{1} to 7.44×10^{7} s^{-1}. In addition, $k_{IC}^{T_1 \rightarrow T_2}$ exceeds both

02 November 2026 09:24:40

Published under an exclusive license by AIP Publishing

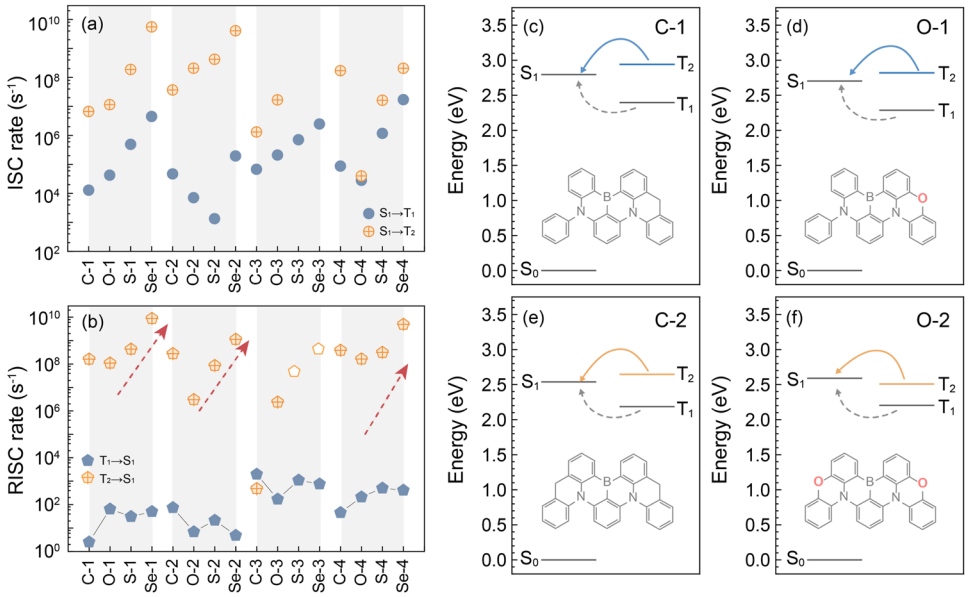


FIG. 3. Multistate T_1/T_2 spin-conversion network and associated rate descriptors for the investigated emitters. (a) Calculated $S_1 \rightarrow T_1$ and $S_1 \rightarrow T_2$ ISC rate constants; (b) calculated $T_1 \rightarrow S_1$ and $T_2 \rightarrow S_1$ RISC rate constants; and [(c)–(f)] representative energy-level diagrams for C-1, O-1, C-2, and O-2, illustrating the T_2-associated spin-conversion pathway. The T_2-related data points for S-3 and Se-3 are omitted from panels (a) and (b) (see Sec. II C).

$k_{rt}^{T_1 \rightarrow S_0}$ and $k_{nrt}^{T_1 \rightarrow S_0}$ for most molecules. These comparisons show that the rapid $T_2 \rightarrow T_1$ IC does not make T_2 inaccessible: T_2 can acquire transient population through direct $S_1 \rightarrow T_2$ ISC and reverse $T_1 \rightarrow T_2$ IC. Nevertheless, the rapid $T_2 \rightarrow T_1$ IC limits productive $T_2 \rightarrow S_1$ RISC branching, so T_2 is an important transient member of the multistate triplet manifold rather than a long-lived reservoir. For 13 of the 14 molecules, $k_{RISC}^{T_2 \rightarrow S_1}$ exceeds $k_{RISC}^{T_1 \rightarrow S_1}$; C-3 is the only exception [Fig. 3(b)]. Thus, T_2 has a stronger intrinsic spin-conversion capability for most molecules, but its state-specific rate must not be equated with the productive branching yield.

The roles of the energy gap and SOC can, thus, be distinguished. The small S_1–T_2 gap is the primary energetic prerequisite for opening a T_2-associated spin-conversion channel, whereas enhanced S_1–T_1 SOC alone cannot compensate for the relatively large S_1–T_1 energy gap. Once the T_2 channel becomes energetically accessible, the SOC magnitude determines how rapidly the spin conversion proceeds. Symmetry breaking enhances the intrinsic $T_2 \rightarrow S_1$ RISC rate, particularly in the X-4 frameworks relative to their X-2 counterparts. However, this enhancement does not necessarily propagate to the effective rate, because the latter additionally depends on the thermal accessibility of the T_2 state, which is dictated by the T_1–T_2 energy gap [Figs. 3(c)–3(f) and S1]. Indeed, the computed k_{RISC}^{eff} values range from 2.65 to 1.05×10^4 s^{-1}, with the maximum value obtained for Se-2. Within the X-2 series, S-2 and Se-2 exhibit the most favorable combination of a relatively small T_1–T_2 gap and a large direct $T_2 \rightarrow S_1$ RISC rate, making Se-2 the emitter with the highest overall effective rate. By contrast, the relatively high effective rate of C-3 is primarily ascribed to its $T_1 \rightarrow S_1$ channel rather than to thermally assisted upconversion via the T_2 state. Overall, symmetry breaking primarily modulates the intrinsic spin-conversion capability through the T_2 manifold, whereas achieving an efficient thermally weighted RISC process requires the synergistic optimization of the T_1–T_2 energy alignment, SOC, and vibronic coupling.

B. Optical spectra

For MR-TADF emitters, RISC acceleration is beneficial only if the narrowband emission character is retained. We, therefore, simulated vibrationally resolved absorption and emission spectra to examine how the structural factors that promote spin conversion also affect color purity. Figures 4(a)–4(f) presents representative calculated spectra for selected C-, O-, and S-containing X-2 and X-3 emitters. These examples were chosen to illustrate characteristic MR-type profiles and to compare the spectral responses of symmetric and asymmetric frameworks. The complete spectra of all 16 emitters, including the X-1, X-4, and Se-containing analogues, are provided in Fig. S4 in the supplementary material. Nevertheless, the emission maximum, Stokes shift, and FWHM vary markedly with both embedded-atom identity and locking configuration, indicating that the spectral response cannot be described by the heavy-atom effect alone. Because these spectra were calculated for isolated molecules in a PCM environment, the absolute FWHM values should not be interpreted as direct predictions of doped-film spectra. Instead, they provide an intrinsic molecular measure of vibronic broadening. This distinction is important because solid-state host polarity, conformational disorder, exciton–phonon coupling, and optical outcoupling can further shift and broaden the measured spectra. The functional benchmark in Table S1 in the supplementary material supports the use of B3LYP/6-311G** for solution-phase emission energies, but it does not constitute a direct validation of absolute film FWHM values. Therefore, the calculated FWHM values are used below to compare relative vibronic broadening within the same computational protocol. Nevertheless, the calculated trends are consistent with representative experiments. Rigid sulfur-containing Cz-PTZ-BN and 2Cz-PTZ-BN retain narrow solution/film emission bandwidths of 37/50 and 38/48 nm, respectively, when the sulfur-containing unit is embedded in a sterically protected framework.[15] Similarly, selenium-containing BN-Se and BNSeSe-based devices maintain electroluminescence FWHM

02 November 2026 09:24:40

Published under an exclusive license by AIP Publishing

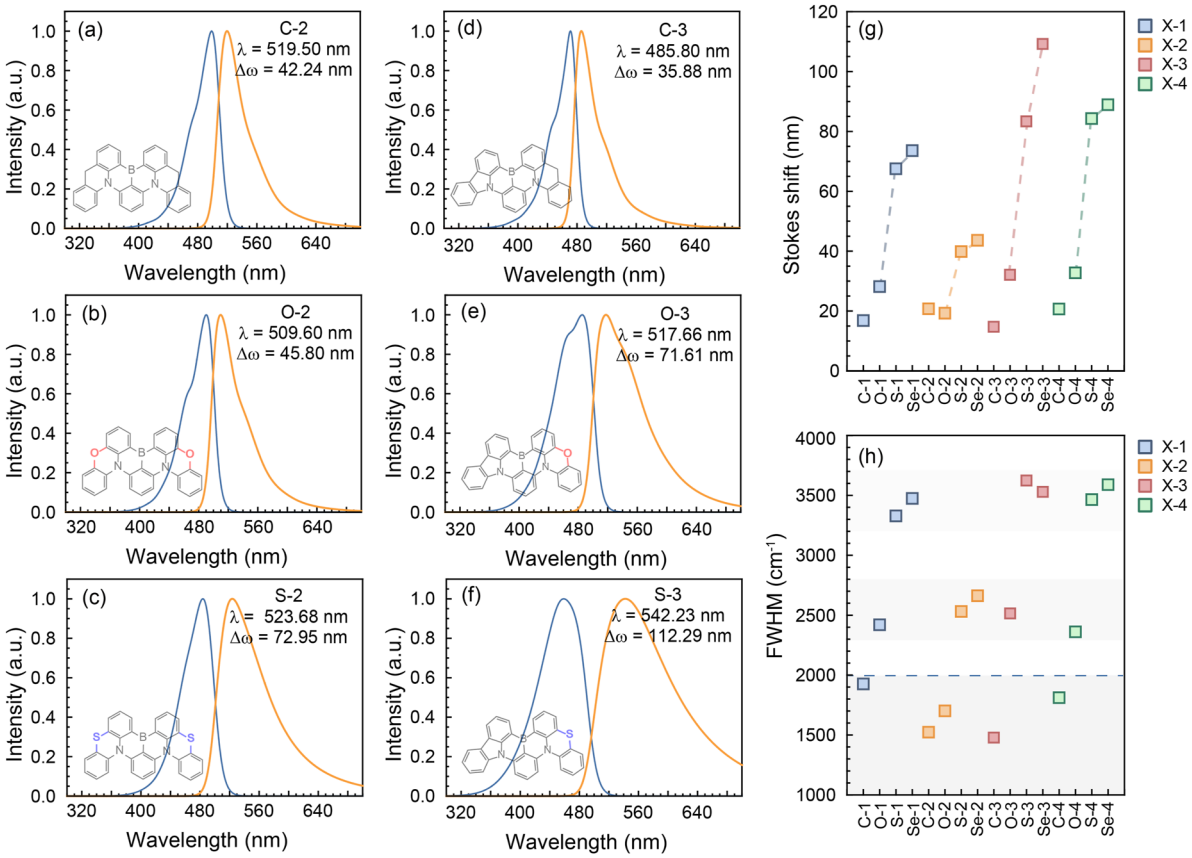


FIG. 4. Optical spectra and emission-broadening correlations. [(a)–(f)] Representative calculated vibrationally resolved absorption and emission spectra of C-2, O-2, S-2, C-3, O-3, and S-3; the blue and orange curves denote absorption and emission spectra, respectively; and the insets show the molecular structure, compound name, calculated emission wavelength (λ), and FWHM for each emitter. (g) Comparison of Stokes shifts and (h) emission FWHM values for different investigated frameworks.

values of about 45–48 nm while showing much faster delayed-fluorescence dynamics.[33,34] These experimental observations agree with the present calculation in a qualitative sense: heavy atoms can accelerate spin conversion, but narrowband emission is preserved only when the molecular framework suppresses S_1/S_0 relaxation and vibronic reorganization.[16,17,25]

The X-2 series in Figs. 4(a)–4(c) illustrates the protective role of the symmetric doubly locked framework. C-2 emits at 519.50 nm with a FWHM of 42.24 nm, and O-2 gives a comparable FWHM of 45.80 nm at 509.60 nm. Thus, replacing C by O in the symmetric framework produces only a limited perturbation of the emissive potential energy surface. In contrast, S-2 emits at 523.68 nm with a broader FWHM of 72.95 nm. This red-shifted and broadened emission indicates that the larger and more polarizable sulfur atom enhances electronic perturbation and structural relaxation, even in a symmetrically locked framework. However, the broadening in S-2 remains much weaker than that in the asymmetric sulfur-containing analogues, indicating that symmetric double locking partly compensates for the color-purity loss caused by heavy-atom embedding.

The influence of the molecular framework becomes more pronounced in the asymmetric X-3 and X-4 series. For X-3, the representative spectra in Figs. 4(d)–4(f) show that the FWHM increases from 35.88 nm for C-3 to 71.61 nm for O-3 and 112.29 nm for S-3, while the emission maximum shifts from 485.80 to 542.23 nm. For X-4, the same trend is observed in the complete spectra in Fig. S4 and the all-emitter comparisons in Figs. 4(g) and 4(h): C-4 remains relatively narrow with a FWHM of 43.31 nm, whereas O-4 and S-4 broaden to 64.01 and 103.80 nm, respectively. These comparisons show that asymmetric locking amplifies the spectral consequences of heteroatom substitution. The heavy atom enhances SOC and the intrinsic high-lying T_2 spin-conversion capability, whereas the asymmetric framework allows larger S_1/S_0 relaxation and stronger vibronic sidebands, producing broader and more red-shifted emission. Therefore, the sulfur effect is not determined by atomic number alone; it is amplified when local heavy-atom perturbation is combined with a less symmetry-balanced molecular framework.

The Stokes-shift and FWHM comparisons in Figs. 4(g) and 4(h) further show that the intrinsic spectral penalty is determined

02 November 2026 09:24:40

Published under an exclusive license by AIP Publishing

by the coupling between heavy-atom embedding and molecular locking configuration. The C and O analogues generally remain in the small-to-moderate broadening region, whereas the S- and Se-containing asymmetric structures occupy the large-Stokes-shift and broad-emission region. The symmetric X-2 framework, especially S-2 and Se-2, lies between these two limits and, therefore, represents a more balanced design: it benefits from heavy-atom-enhanced spin conversion while avoiding the severe spectral broadening of X-3 and X-4. Together with the RISC analysis in Fig. 2 and the mechanistic picture in Fig. 3, these spectra reveal a clear separation of roles. The high-lying T_2 state contributes to the intrinsic spin-conversion capability within the multistate network, whereas the rigidity, symmetry, and relaxation of the S_1 potential energy surface determine whether narrowband MR emission is preserved. These results indicate that heavy atoms should be introduced into a locally effective but globally rigid framework to enhance SOC without excessive loss of intrinsic emission color purity.

C. Vibronic coupling

The origin of spectral broadening can be traced to S_1/S_0 structural relaxation and the associated electron–vibration coupling. The calculated molecular geometries are shown in Table S3; because the structures undergo relatively large relaxation, the structural changes cannot be described solely by variations in selected bond lengths and bond angles. We first compared the RMSD values between optimized S_0 and S_1 geometries. As shown in Table I and Fig. S5, double locking generally suppresses excited-state structural relaxation. The symmetric X-2 structures have the smallest RMSD values in each atom series, ranging from 0.069 to 0.078 Å. By contrast, asymmetric heavy-atom structures relax more strongly; S-3 and Se-3 reach RMSD values of 0.163 and 0.171 Å, respectively. This trend explains why symmetric double locking preserves color purity, whereas asymmetric S and Se embedding tends to broaden emission.

The RMSD descriptor, however, does not fully determine the emission bandwidth. The $S_1 \rightarrow S_0$ reorganization energy (Γ) provides a more direct energetic measure of the relaxation between the emissive and ground-state potential energy surfaces. The C and O series have moderate reorganization energies of 937–1398 cm^{-1}, whereas the S and Se asymmetric structures show much larger values. The largest values appear for S-3, Se-3, S-4, and Se-4, all close to or above 2100 cm^{-1}. In contrast, S-2 and Se-2 remain at 1132 and 1152 cm^{-1}, respectively, again highlighting the protective role of symmetric double locking. This distinction is further quantified in Figs. 5(a) and 5(b). The RMSD–FWHM distribution in Fig. 5(a) indicates that large structural displacement usually accompanies increased emission bandwidth, but the points do not follow a strict linear relationship. Therefore, a global geometrical descriptor alone is not sufficient to predict the emission bandwidth. By contrast, Fig. 5(b) demonstrates that the FWHM correlates much more closely with the $S_1 \rightarrow S_0$ reorganization energy, with $R^2 = 0.87$. Thus, the energetic cost of S_1/S_0 relaxation is a more direct predictor of intrinsic molecular emission broadening than the total RMSD. The same descriptor relationship was also emphasized by Li and Shuai, who reported a robust correlation between emission-state reorganization energy and FWHM within a related TVCF-based protocol.[68] This agreement indicates that the reorganization-energy control of emission bandwidth has a degree of generality across sulfur/selenium-containing MR-TADF frameworks.

The nearly identical vertical emission energies and total reorganization energies of S-3 and Se-3, despite their markedly different vibronic emission maxima, further indicate that the peak position of such broad spectra is governed by the detailed distribution of vibronic intensity rather than by the electronic energy gap or total reorganization energy alone. Therefore, mode-resolved Huang–Rhys factor analysis further clarifies the microscopic origin of emission broadening. The complete mode-resolved Huang–Rhys factor and reorganization-energy distributions are provided in Fig. S6 in the supplementary material. As shown in Figs. 5(c)–5(e), for C-2, O-2, and S-2, the total reorganization energies are 972.45, 983.92, and 1132.14 cm^{-1}, respectively, and the dominant vibronic contributions are concentrated in low-frequency modes near 80–104 cm^{-1}. These moderate reorganization energies are consistent with their relatively narrow or moderately broadened emission profiles. In contrast, the asymmetric X-3 framework displays a much stronger dependence on the embedded atom. As shown in Figs. 5(f)–5(h), the total reorganization energy increases from 936.72 cm^{-1} for C-3 to 1398.33 cm^{-1} for O-3 and 2181.82 cm^{-1} for S-3. For S-3, additional low-frequency modes at 27.51 and 69.82 cm^{-1} make large contributions, indicating that soft structural deformation is strongly coupled to the $S_1 \rightarrow S_0$ emission process.

These results establish that the calculated molecular emission bandwidth is governed not only by the magnitude of the overall structural displacement but more directly by the reorganization energy and its distribution over active vibrational

TABLE I. RMSD values between S_0 and S_1 geometries and $S_1 \rightarrow S_0$ reorganization energies (Γ).

Molecule	RMSD/Å	$\Gamma_{S_1 \rightarrow S_0}/cm^{-1}$	Molecule	RMSD/Å	$\Gamma_{S_1 \rightarrow S_0}/cm^{-1}$
C-1	0.124	968	C-3	0.092	937
O-1	0.125	1192	O-3	0.109	1398
S-1	0.148	1720	S-3	0.163	2182
Se-1	0.157	1805	Se-3	0.171	2178
C-2	0.072	972	C-4	0.086	1055
O-2	0.069	984	O-4	0.090	1341
S-2	0.078	1132	S-4	0.140	2114
Se-2	0.077	1152	Se-4	0.149	2197

02 November 2026 09:24:40

Published under an exclusive license by AIP Publishing

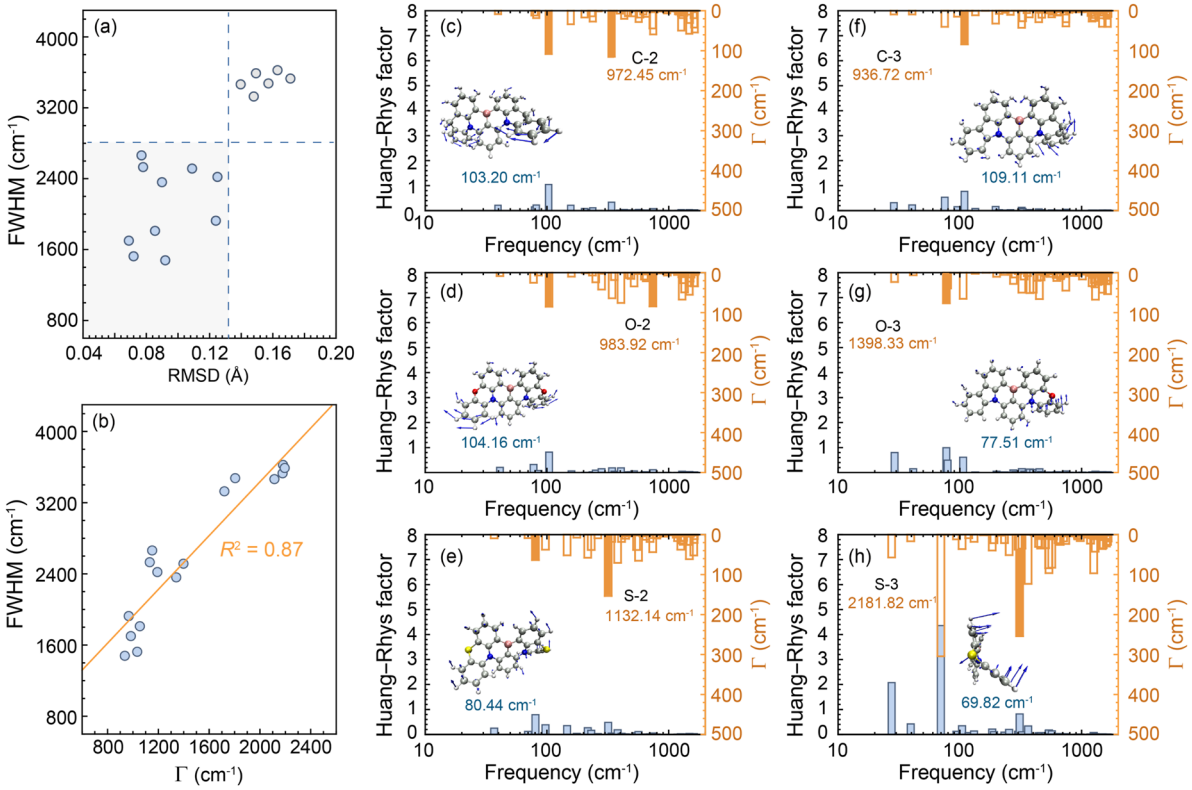


FIG. 5. Vibronic coupling and reorganization-energy analysis. (a) Relationship between emission FWHM and RMSD; (b) linear correlation between emission FWHM and $S_1 \rightarrow S_0$ reorganization energy (Γ); and [(c)–(h)] Huang–Rhys factors and mode-resolved reorganization-energy contributions (Γ) for representative C-, O-, and S-containing emitters.

modes.[17,56] Together with the RISC analysis, these results reveal the central efficiency–color-purity trade-off. Asymmetric heavy-atom-containing structures are favorable for strengthening SOC and increasing the intrinsic high-lying-triplet spin-conversion rates, but the productive contribution of this channel remains subject to $T_2 \rightarrow T_1$ internal conversion; these structures also enhance structural relaxation and vibronic coupling, leading to larger Stokes shifts and broader emission. Symmetric double locking is, therefore, essential for retaining color purity because it limits excited-state relaxation while retaining a favorable multistate T_1/T_2 spin-conversion network. Thus, localized heavy-atom-induced SOC enhancement should be combined with rigid framework locking to strengthen intrinsic spin conversion without excessive loss of emission color purity.

Overall, the conclusions drawn here should be interpreted as internally consistent molecular-level trends rather than absolute device predictions. The B3LYP benchmark supports the description of emission energies for related solution-phase emitters, the T_2 assignment is an operational description of the low-lying triplet manifold, and the Se/S SOC values are used as comparative descriptors within one basis-set and SOC protocol. With these qualifications, the same qualitative picture emerges from independent descriptors: near-resonant S_1/T_2 alignment and enhanced SOC promote RISC, whereas structural relaxation and reorganization energy determine whether narrowband emission can be retained.

IV. CONCLUSION

In conclusion, this work demonstrates that the efficiency–color-purity balance of heavy-atom-modified B/N MR-TADF emitters is governed by the coupling between high-lying-triplet spin-conversion dynamics and excited-state structural relaxation. Chalcogen embedding and framework symmetry breaking cooperatively tune the T_2 orbital character and enhance the intrinsic $T_2 \rightarrow S_1$ RISC rate constants. However, the $T_2 \leftrightarrow T_1$ IC analysis reveals that the direct $T_2 \rightarrow S_1$ process is uniformly slower than the competing $T_2 \rightarrow T_1$ IC, indicating that T_2 serves as a transient intermediate within the kinetic network rather than as a dominant productive channel. Consequently, although symmetry breaking can promote the intrinsic $T_2 \rightarrow S_1$ RISC rate, achieving an efficient thermally weighted RISC process requires the synergistic optimization of the T_1–T_2 energy alignment, SOC, and vibronic coupling. Simultaneously, excessive framework asymmetry and heavy-atom perturbation increase S_1/S_0 reorganization and broaden the emission, with the calculated FWHM correlating more closely with reorganization energy than with global RMSD. These findings suggest that the color purity and efficiency of MR-TADF emitters should combine

02 November 2026 09:24:40

Published under an exclusive license by AIP Publishing

localized SOC enhancement with a rigid, symmetry-balanced framework, so that S_1–T_2 energy alignment, SOC, framework rigidity, and $S_1 \rightarrow S_0$ reorganization energy are optimized simultaneously.

SUPPLEMENTARY MATERIAL

See the supplementary material for the functional benchmark and statistical errors of the calculated emission energies (Table S1); the T_1- and T_2-related ISC and RISC descriptors, including adiabatic energy gaps, SOC matrix elements for the forward ISC and reverse RISC directions, the corresponding rate constants, effective RISC rate constants, and triplet-state radiative, nonradiative, and IC rate constants at 300 K (Table S2); the energy-level distributions of the low-lying excited states (Fig. S1); NTO and state-character analyses (Figs. S2 and S3); vibrationally resolved absorption and emission spectra (Fig. S4); optimized molecular geometries and RMSD analysis (Table S3 and Fig. S5); mode-resolved vibronic coupling (Fig. S6); and Cartesian coordinates of the ground-state structures (Table S4).

ACKNOWLEDGMENTS

Y.W. acknowledges support from the Young Scientists Fund of the National Natural Science Foundation of China (NSFC) (Grant No. 22503077) and the China Postdoctoral Science Foundation (Grant No. 2025M771052). This work was also supported by the National Natural Science Foundation of China (Grant Nos. T2350009 and 22433007), the Guangdong Provincial Natural Science Foundation (Grant No. 2024A1515011185), and the Shenzhen City Peacock Team Project (Grant No. KQTD20240729102028011). Y.W. acknowledges the computational resources used in this work and thanks colleagues for helpful discussions. Y.W. is also grateful to Reviewer 2 for the thorough and constructive comments, which helped identify inconsistencies and significantly improved the quality of the manuscript.

AUTHOR DECLARATIONS

Conflict of Interest

The authors have no conflicts to disclose.

Author Contributions

Yaxin Wang: Conceptualization (equal); Data curation (equal); Formal analysis (equal); Funding acquisition (equal); Resources (equal); Validation (equal); Visualization (equal); Writing – original draft (equal). **Wensheng Yang**: Funding acquisition (equal); Resources (equal); Supervision (equal). **Xiaonan Ma**: Data curation (equal); Formal analysis (equal); Funding acquisition (equal); Resources (equal); Writing – review & editing (equal). **Zhigang Shuai**: Funding acquisition (equal); Methodology (equal); Resources (equal); Software (equal); Supervision (equal); Writing – review & editing (equal).

DATA AVAILABILITY

The data that support the findings of this study are available within the article and its supplementary material. Additional computational data are available from the corresponding author upon reasonable request.

REFERENCES

[1] C. W. Tang and S. A. VanSlyke, Appl. Phys. Lett. **51**, 913 (1987).
[2] Y. Huang, E.-L. Hsiang, M.-Y. Deng, and S.-T. Wu, Light: Sci. Appl. **9**, 105 (2020).
[3] J. Song, H. Lee, E. G. Jeong, K. C. Choi, and S. Yoo, Adv. Mater. **32**, 1907539 (2020).
[4] G. Hong, X. Gan, C. Leonhardt, Z. Zhang, J. Seibert, J. M. Busch, and S. Bräse, Adv. Mater. **33**, 2005630 (2021).
[5] T. Hua, X. Cao, J. Miao, X. Yin, Z. Chen, Z. Huang, and C. Yang, Nat. Photonics **18**, 1161 (2024).
[6] H. Uoyama, K. Goushi, K. Shizu, H. Nomura, and C. Adachi, Nature **492**, 234 (2012).
[7] S. Hirata, Y. Sakai, K. Masui, H. Tanaka, S. Y. Lee, H. Nomura, N. Nakamura, M. Yasumatsu, H. Nakanotani, Q. Zhang, K. Shizu, H. Miyazaki, and C. Adachi, Nat. Mater. **14**, 330 (2015).
[8] Z. Yang, Z. Mao, Z. Xie, Y. Zhang, S. Liu, J. Zhao, J. Xu, Z. Chi, and M. P. Aldred, Chem. Soc. Rev. **46**, 915 (2017).
[9] Y. Liu, C. Li, Z. Ren, S. Yan, and M. R. Bryce, Nat. Rev. Mater. **3**, 18020 (2018).
[10] J. M. Dos Santos, D. Hall, B. Basumatary, M. Bryden, D. Chen, P. Choudhary, T. Comerford, E. Crovini, A. Danos, J. De, S. Diesing, M. Fatahi, M. Griffin, A. K. Gupta, H. Hafeez, L. Hämmerling, E. Hanover, J. Haug, T. Heil, D. Karthik, S. Kumar, O. Lee, H. Li, F. Lucas, C. F. R. Mackenzie, A. Mariko, T. Matulaitis, F. Millward, Y. Olivier, Q. Qi, I. D. W. Samuel, N. Sharma, C. Si, L. Spierling, P. Sudhakar, D. Sun, E. Tankelevičiutė, M. Duarte Tonet, J. Wang, T. Wang, S. Wu, Y. Xu, L. Zhang, and E. Zysman-Colman, Chem. Rev. **124**, 13736 (2024).
[11] M. A. Baldo, D. F. O'Brien, Y. You, A. Shoustikov, S. Sibley, M. E. Thompson, and S. R. Forrest, Nature **395**, 151 (1998).
[12] X.-K. Chen, D. Kim, and J.-L. Brédas, Acc. Chem. Res. **51**, 2215 (2018).
[13] L.-S. Cui, A. J. Gillett, S.-F. Zhang, H. Ye, Y. Liu, X.-K. Chen, Z.-S. Lin, E. W. Evans, W. K. Myers, T. K. Ronson, H. Nakanotani, S. Reineke, J.-L. Bredas, C. Adachi, and R. H. Friend, Nat. Photonics **14**, 636 (2020).
[14] X. Wu, J.-W. Huang, B.-K. Su, S. Wang, L. Yuan, W.-Q. Zheng, H. Zhang, Y.-X. Zheng, W. Zhu, and P.-T. Chou, Adv. Mater. **34**, 2105080 (2022).
[15] F. Liu, Z. Cheng, Y. Jiang, L. Gao, H. Liu, H. Liu, Z. Feng, P. Lu, and W. Yang, Angew. Chem., Int. Ed. **61**, e202116927 (2022).
[16] Y. Wang, Z. Guo, Y. Gao, Y. Tian, Y. Deng, X. Ma, and W. Yang, J. Phys. Chem. Lett. **13**, 6664 (2022).
[17] Y. Gao, Y. Wang, Z. Guo, Y. Wan, Z. Xue, Y. Han, W. Yang, and X. Ma, Chem. Sci. **15**, 6410 (2024).
[18] T. Hatakeyama, K. Shiren, K. Nakajima, S. Nomura, S. Nakatsuka, K. Kinoshita, J. Ni, Y. Ono, and T. Ikuta, Adv. Mater. **28**, 2777 (2016).
[19] Y. Kondo, K. Yoshiura, S. Kitera, H. Nishi, S. Oda, H. Gotoh, Y. Sasada, M. Yanai, and T. Hatakeyama, Nat. Photonics **13**, 678 (2019).
[20] S. M. Suresh, D. Hall, D. Beljonne, Y. Olivier, and E. Zysman-Colman, Adv. Funct. Mater. **30**, 1908677 (2020).
[21] K. R. Naveen, H. I. Yang, and J. H. Kwon, Commun. Chem. **5**, 149 (2022).
[22] D. H. Ahn, S. W. Kim, H. Lee, I. J. Ko, D. Karthik, J. Y. Lee, and J. H. Kwon, Nat. Photonics **13**, 540 (2019).
[23] M. Yang, I. S. Park, and T. Yasuda, J. Am. Chem. Soc. **142**, 19468 (2020).
[24] J.-M. Teng, Y.-F. Wang, and C.-F. Chen, J. Mater. Chem. C **8**, 11340 (2020).
[25] Y. Gao, Y. Wang, Z. Guo, Y. Wan, C. Li, B. Yang, W. Yang, and X. Ma, J. Phys. Chem. B **126**, 2729 (2022).
[26] Y. Wang, Y. Tian, Y. Gao, Z. Guo, Z. Xue, Y. Han, W. Yang, and X. Ma, J. Phys. Chem. Lett. **14**, 9665 (2023).
[27] Y. Wang and Z. Shuai, J. Phys. Chem. Lett. **16**, 7752 (2025).
[28] Q. Zhang, T. Liu, Z. Shi, Z. Zheng, C. Lv, X. Wang, and Y. Zhang, Phys. Chem. Chem. Phys. **26**, 5147 (2024).
[29] K. Shizu and H. Kaji, Nat. Commun. **15**, 4723 (2024).
[30] I. S. Park, K. Matsuo, N. Aizawa, and T. Yasuda, Adv. Funct. Mater. **28**, 1802031 (2018).

02 November 2026 09:24:40

Published under an exclusive license by AIP Publishing

[31] F. Chen, L. Zhao, X. Wang, Q. Yang, W. Li, H. Tian, S. Shao, L. Wang, X. Jing, and F. Wang, Sci. China: Chem. **64**, 547 (2021).
[32] T. Hua, L. Zhan, N. Li, Z. Huang, X. Cao, Z. Xiao, S. Gong, C. Zhou, C. Zhong, and C. Yang, Chem. Eng. J. **426**, 131169 (2021).
[33] X. Cao, K. Pan, J. Miao, X. Lv, Z. Huang, F. Ni, X. Yin, Y. Wei, and C. Yang, J. Am. Chem. Soc. **144**, 22976 (2022).
[34] Y. X. Hu, J. Miao, T. Hua, Z. Huang, Y. Qi, Y. Zou, Y. Qiu, H. Xia, H. Liu, X. Cao, and C. Yang, Nat. Photonics **16**, 803 (2022).
[35] Y. Chang, Y. Wu, X. Wang, W. Li, Q. Yang, S. Wang, S. Shao, and L. Wang, Chem. Eng. J. **451**, 138545 (2023).
[36] I. S. Park, H. Min, and T. Yasuda, Angew. Chem., Int. Ed. **61**, e202205684 (2022).
[37] S. M. Pratik, V. Coropceanu, and J.-L. Brédas, Chem. Mater. **34**, 8022 (2022).
[38] P. Yang, J. H. Lee, K. Urano, and T. Yasuda, Angew. Chem., Int. Ed. **65**, e24098 (2026).
[39] Y. Qi, W. Ning, Y. Zou, X. Cao, S. Gong, and C. Yang, Adv. Funct. Mater. **31**, 2102017 (2021).
[40] Y. Zhang, D. Zhang, T. Huang, A. J. Gillett, Y. Liu, D. Hu, L. Cui, Z. Bin, G. Li, J. Wei, and L. Duan, Angew. Chem., Int. Ed. **60**, 20498 (2021).
[41] X. Lv, J. Miao, M. Liu, Q. Peng, C. Zhong, Y. Hu, X. Cao, H. Wu, Y. Yang, C. Zhou, J. Ma, Y. Zou, and C. Yang, Angew. Chem., Int. Ed. **61**, e202201588 (2022).
[42] S. Oda, B. Kawakami, Y. Yamasaki, R. Matsumoto, M. Yoshioka, D. Fukushima, S. Nakatsuka, and T. Hatakeyama, J. Am. Chem. Soc. **144**, 106 (2022).
[43] P. Jiang, J. Miao, X. Cao, H. Xia, K. Pan, T. Hua, X. Lv, Z. Huang, Y. Zou, and C. Yang, Adv. Mater. **34**, 2106954 (2022).
[44] Y. Zhang, J. Wei, D. Zhang, C. Yin, G. Li, Z. Liu, X. Jia, J. Qiao, and L. Duan, Angew. Chem., Int. Ed. **61**, e202113206 (2022).
[45] Y. Xu, Q. Wang, J. Wei, X. Peng, J. Xue, Z. Wang, S.-J. Su, and Y. Wang, Angew. Chem., Int. Ed. **61**, e202204652 (2022).
[46] Y. Zhang, G. Li, L. Wang, T. Huang, J. Wei, G. Meng, X. Wang, X. Zeng, D. Zhang, and L. Duan, Angew. Chem., Int. Ed. **61**, e202202380 (2022).
[47] X. Cai, Y. Pu, C. Li, Z. Wang, and Y. Wang, Angew. Chem., Int. Ed. **62**, e202304104 (2023).
[48] Q. Wang, Y. Xu, T. Huang, Y. Qu, J. Xue, B. Liang, and Y. Wang, Angew. Chem., Int. Ed. **62**, e202301930 (2023).
[49] H. Min, I. S. Park, and T. Yasuda, Angew. Chem., Int. Ed. **60**, 7643 (2021).
[50] S. Wu, A. K. Gupta, K. Yoshida, J. Gong, D. Hall, D. B. Cordes, A. M. Z. Slawin, I. D. W. Samuel, and E. Zysman-Colman, Angew. Chem., Int. Ed. **61**, e202213697 (2022).
[51] A. Pershin, D. Hall, V. Lemaur, J. C. Sancho-Garcia, L. Muccioli, E. Zysman-Colman, D. Beljonne, and Y. Olivier, Nat. Commun. **10**, 597 (2019).
[52] Y.-J. Pu, D. Valverde, J. C. Sancho-García, and Y. Olivier, J. Phys. Chem. A **127**, 10189 (2023).
[53] D. Valverde, C. T. Ser, G. Ricci, K. Jorner, R. Pollice, A. Aspuru-Guzik, and Y. Olivier, ACS Appl. Mater. Interfaces **16**, 66991 (2024).
[54] Y. Gao, Y. Sun, Z. Guo, G. Yu, Y. Wang, Y. Wan, Y. Han, W. Yang, D. Zhao, and X. Ma, Chem. Sci. **15**, 18431 (2024).
[55] Z. Guo, Y. Wang, J. Heitmüller, C. Sieck, A. Prüfer, P. Ralle, A. Steffen, P. Henke, P. R. Ogilby, T. B. Marder, X. Ma, and T. Brixner, Chem. Sci. **15**, 14746 (2024).
[56] Z. Guo, P. Liu, Y. Sha, Y. Gao, G. Yu, H.-H. Lv, Y. Wang, Y. Han, W. Yang, X.-Y. Wang, and X. Ma, J. Phys. Chem. Lett. **16**, 4615 (2025).
[57] Q. Peng, Y. Yi, Z. Shuai, and J. Shao, J. Am. Chem. Soc. **129**, 9333 (2007).
[58] Y.-L. Niu, Q. Peng, C.-M. Deng, X. Gao, and Z. Shuai, Sci. China, Ser. B: Chem. **51**, 1153 (2008).
[59] Q. Peng, Y. Yi, Z. Shuai, and J. Shao, J. Chem. Phys. **126**, 114302 (2007).
[60] Y.-L. Niu, Q. Peng, C. Deng, X. Gao, and Z. Shuai, J. Phys. Chem. A **114**, 7817 (2010).
[61] Q. Peng, D. Fan, R. Duan, Y. Yi, Y. Niu, D. Wang, and Z. Shuai, J. Phys. Chem. C **121**, 13448 (2017).
[62] Y. Niu, W. Li, Q. Peng, H. Geng, Y. Yi, L. Wang, G. Nan, D. Wang, and Z. Shuai, Mol. Phys. **116**, 1078 (2018).
[63] Z. Shuai, Chin. J. Chem. **38**, 1223 (2020).
[64] M. J. Frisch, G. W. Trucks, H. B. Schlegel, G. E. Scuseria, M. A. Robb, J. R. Cheeseman, G. Scalmani, V. Barone, G. A. Petersson, H. Nakatsuji, X. Li, M. Caricato, A. V. Marenich, J. Bloino, B. G. Janesko, R. Gomperts, B. Mennucci, H. P. Hratchian, J. V. Ortiz, A. F. Izmaylov, J. L. Sonnenberg, D. Williams-Young, F. Ding, F. Lipparini, F. Egidi, J. Goings, B. Peng, A. Petrone, T. Henderson, D. Ranasinghe, V. G. Zakrzewski, J. Gao, N. Rega, G. Zheng, W. Liang, M. Hada, M. Ehara, K. Toyota, R. Fukuda, J. Hasegawa, M. Ishida, T. Nakajima, Y. Honda, O. Kitao, H. Nakai, T. Vreven, K. Throssell, J. A. Montgomery, J. E. Peralta, F. Ogliaro, M. J. Bearpark, J. J. Heyd, E. N. Brothers, K. N. Kudin, V. N. Staroverov, T. A. Keith, R. Kobayashi, J. Normand, K. Raghavachari, A. P. Rendell, J. C. Burant, S. S. Iyengar, J. Tomasi, M. Cossi, J. M. Millam, M. Klene, C. Adamo, R. Cammi, J. W. Ochterski, R. L. Martin, K. Morokuma, O. Farkas, J. B. Foresman, and D. J. Fox, *Gaussian 16, Revision C.01*, Gaussian, Inc., Wallingford, CT, 2016, see also https://gaussian.com.
[65] D. Hall, J. C. Sancho-García, A. Pershin, G. Ricci, D. Beljonne, E. Zysman-Colman, and Y. Olivier, J. Chem. Theory Comput. **18**, 4903 (2022).
[66] X. Gao, S. Bai, D. Fazzi, T. Niehaus, M. Barbatti, and W. Thiel, J. Chem. Theory Comput. **13**, 515 (2017).
[67] T. Lu and F. Chen, J. Comput. Chem. **33**, 580 (2012).
[68] R. Li and Z. Shuai, J. Chem. Phys. **163**, 234302 (2025).

02 November 2026 09:24:40

Published under an exclusive license by AIP Publishing